Enabling In-Situ Magnetic Interference Mitigation Algorithm Validation via a Laboratory-Generated Dataset

Matthew G. Finley[1,3,4], Allison M. Flores[2], Katherine J. Morris[1], Robert M. Broadfoot[1], Sam Hisel[1], Jason Homann[1], Chris Piker[1], Ananya Sen Gupta[2], and David M. Miles[1]

5 [1]Department of Physics and Astronomy, University of Iowa, Iowa City, IA, USA
[2]Department of Electrical and Computer Engineering, University of Iowa, Iowa City, IA, USA
[3]Geospace Physics Laboratory, Goddard Space Flight Center, NASA, Greenbelt, MD, USA
[4]Department of Astronomy, University of Maryland, College Park, MD, USA

Correspondence to: Matthew G. Finley (matthew.g.finley@nasa.gov)

10 **Abstract.** Magnetometer measurements are one of the critical components necessary to improve our understanding of the intricate physical processes coupling mass, momentum, and energy within near-Earth space and throughout our solar system. However, these measurements are often contaminated by stray magnetic fields from the spacecraft hosting the magnetic field sensors, and the data often requires the application of interference mitigation algorithms prior to scientific use. Rigorous numerical validation of these techniques can be challenging when they are applied to in-situ spaceflight data, as a ground truth for the local magnetic field is often unavailable. This manuscript introduces and details the generation of an open-source dataset designed to facilitate

15 the assessment of interference mitigation techniques for magnetic field data collected during spaceflight missions. The dataset contains over 100 hours of magnetic field data comprising mixtures of near-DC trends, physically-synthesized interference, and pseudo-geophysical phenomena. These constituent source signals have been independently captured by four synchronized magnetometers sampling at high cadence and combined into 30-minute intervals of data representative of events and interference seen in historic missions. The physical location of the four magnetometers relative to the interference sources enables researchers to test their interference mitigation algorithms with various magnetometer suite configurations, and the dataset also provides a ground truth for

20 the underlying interference signals, enabling rigorous quantification of the results of past, present, and future interference mitigation efforts.

1 Introduction

In-situ magnetometer measurements are a vital component to our search in understanding the various physical processes that couple mass, momentum, and energy throughout near-Earth space and our solar system. Magnetometers have been used to collect scientific data since the first days of humanity's exploration of space. Early missions such as Sputnik 3,

25 Pioneer 1, and Explorer 6 all carried scientific magnetometers (Gordon & Brown, 1972). Since then, many advancements have been made to the science of triaxial spaceflight magnetometer design and implementation, enabling magnetometer suites capable of making measurements from Mars (Connerney et al., 2015) to the harsh radiation environment around Jupiter (Connerney et al., 2017) to the sun itself (Bale et al., 2016). Novel manufacturing processes now provide bespoke ferromagnetic fluxgate cores (Miles et al., 2019) and allow unique magnetometer topologies suitable for applications such as

30 large constellations of nanosatellites (Greene et al., 2022).

Regardless of the improvements made to the magnetic field sensors themselves, magnetometer measurements are often contaminated by stray magnetic fields emanating from the spacecraft on which they are deployed. These interference

sources can include the battery and solar panel systems used to provide the spacecraft's power, the reaction wheels and magnetorquers used to control the spacecraft's attitude, and even the ferromagnetic materials used in the construction of the spacecraft itself (e.g., Broadfoot et al., 2022; Stolle et al., 2021; Styp-Rekowski et al., 2022). Historically, this interference has been mitigated by placing the magnetic field sensor at the end of a long boom, increasing the physical distance from the spacecraft and its associated magnetic noise sources. An additional technique for reducing the impact of the stray fields deploys multiple magnetometers at different distances along the boom; the resulting magnetic gradient between the two sensors can be fit to an ideal dipole (or multipole, if necessary) and removed from the original measurements, resulting in improved data fidelity (Ness et al., 1971).

Although this standard gradiometric approach has seen success on a wide variety of missions, it relies on long booms to achieve optimal performance. Historic missions such as MAGSAT and Voyager have seen boom lengths ranging from 6 to 13 meters (Langel et al., 1982; Miller, 1979). To reduce the cost and complexity associated with magnetic field measurements, many modern missions now utilize shorter booms. For example: Parker Solar Probe has fluxgate magnetometers deployed up to 2.7 meters from the host spacecraft (Bale et al., 2016) and CASSIOPE/Swarm-Echo operates with a 0.9-meter boom (Wallis et al., 2015). Even though these short booms reduce mission cost and technical complexity, they diminish the effectiveness of the standard gradiometric interference mitigation approach, especially in the case where the dominating interference is caused by time-varying sources such as reaction wheels. This is because the reduced separation from the spacecraft places the sensors in the interference source's near-field, meaning complex multi-pole terms can no longer be ignored. Multi-pole models can be generated to remove the time-varying interference, but these models often prove challenging to develop due to their requirement of exhaustive pre-flight characterization of all possible interference sources.

The desire for high-fidelity magnetic field data with limited boom length has recently led to the development of a variety of new approaches for the mitigation of local magnetic interference. These new techniques range from unique magnetometer configurations – such as the DAGR instrument on the Dellingr cube satellite (Clagett et al., 2017) and the NEMISIS instrument on the Lunar Gateway HERMES suite (Burt et al., 2022; Paterson et al., 2023) – to the development of new algorithms for interference identification and removal (Bowen et al., 2020; Constantinescu et al., 2020; Finley, Bowen, et al., 2023; Finley, Broadfoot, et al., 2023; Hoffmann & Moldwin, 2022; Imajo et al., 2021; Sen Gupta & Miles, 2023). The performance of the interference mitigation offered by these techniques, however, is often difficult to rigorously quantify due to the unavailability of ground-truth data from in-situ measurements.

This manuscript provides details of an open source, laboratory generated dataset intended to enable numerical analysis of existing and future interference mitigation techniques for in-situ magnetic field data. Specifically, ~10 hours of magnetic field data from four sensors in a practical configuration have been captured. The resulting dataset contains data exhibiting large near-DC trends, physically synthesized reaction wheel interference, and pseudo-geomagnetic phenomena. Further, each measurement interval of these three broad data categories were captured individually prior to their combination, effectively providing a ground-truth for the magnetic interference and residual geophysical fields, such that the performance of interference mitigation techniques can be rigorously quantified. Additionally, the method of data combination used in this

manuscript can result in >120 hours of unique field measurements suitable for testing a variety of data-intensive algorithms such as those provided by machine learning techniques.

Section 2 will detail the physical apparatus used to provide magnetic stimulus and capture magnetic field data. Section 3 will explain the stimulus applied to generate the three data subsets (i.e., interference, geomagnetic phenomena, and low-frequency trend), the filtering and additional steps taken to provide the combined result, and will show several examples of the combined data product. Section 4 will discuss potential limitations of the dataset and avenues for future work. Finally, Sec. 5 will summarize and conclude this manuscript.

2 Apparatus

This section describes the physical apparatus used to produce the dataset described in this manuscript.

2.1 Magnetometers

The magnetic field sensors used for data acquisition as part of this effort are commercially available magnetoresistive vector magnetometers (VMR) produced by Twinleaf LLC. These triaxial sensors have a sensitivity of 300 pT/Hz$^{1/2}$ with a linear field range of ±100,000 nT and are assumed to be calibrated out of the box. Four of these Twinleaf VMR sensors were synchronized and sampled at 200 Hz using the Twinleaf SYNC4 networking hub and associated Twinleaf I/O software. Figure 1 shows one of these magnetometers.
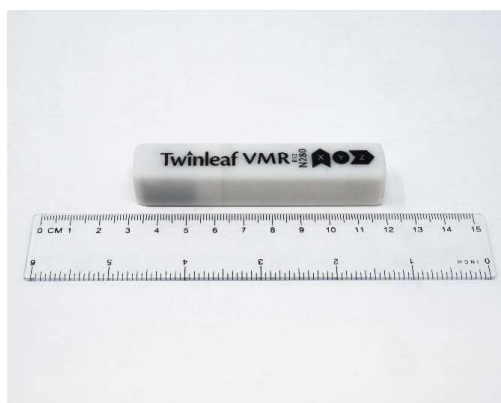
Figure 1: Twinleaf VMR magnetometer used in the generation of this dataset.

2.2 Merritt Coil

The apparatus used to simulate large near-DC magnetic fields is a 2-meter cubic 3-axis Merritt coil system (Merritt et al., 1983) shown in Fig. 2. This coil system was manufactured by Serviciencia (model BM4-2000-3-A). For the collection

of this dataset the coil system was connected to a Bartington PA-1 power amplifier and CU-1 control unit. The coil system has a field homogeneity of ±1% in a cube with sides of ~1-meter and can sustain a maximum steady field of ±0.9 mT. The signal

90   generated by the coil control software is limited by the resolution of the signal generator and, per the instruction manual, has difficulty generating signals lower than 1 Hz. Signals generated at frequencies lower than ~1 Hz will exhibit significant amplitude discontinuities. However, simple filtering can be applied after data collection to mitigate the amplitude stepping in such cases. Data processing is discussed in greater detail in Sec. 3.2.

The coils are constructed to avoid creating conducting loops in the coil formers that could induce eddy currents,
95   allowing for the formers to operate as single loop AC stimulus coils separately from the system. This utility allows for interesting time-varying pseudo-geomagnetic fields, such as wave packets and chirps, to be applied inside the coil via a function generator (in this case, an SRS DS360 Ultra Low Distortion Function Generator). Note that the coil system was operated in an open-loop configuration, meaning that there was no activate compensation being applied to cancel the local magnetic fields. This serves to enhance the complexity of these synthetic geophysical fields by introducing fields from local
100   magnetic phenomena.

Figure 2: Merritt coil system used to simulate various geophysical signals.

2.3 Interference Sources

The primary objective of this effort was to simulate magnetic interference from sources that are often difficult to
105   characterize and remove, while maintaining an observable ground truth for numerical validation. Spacecraft are often contaminated by time-varying magnetic interference from the spinning reaction wheels used to control the vehicle's attitude. These ferromagnetic platters often rotate at rates between 2 Hz (e.g., Parker Solar Probe (Bowen et al., 2020)) and 15 Hz (e.g.,

Swarm-Echo (Wallis et al., 2015)). To simulate these reaction wheels two Greartisan ZGB37RG 12 V_{DC} 1000 RPM (~17 Hz) electric motors were used to rotate 3D-printed plates with inset 3/8" cast iron strips. Figure 3 shows the motor with rotating plate attached.

110

Figure 3: Low-frequency motor and attached plate with inset cast iron strips, designed to simulate spacecraft reaction wheels.

2.4 Integrated Apparatus

To ensure consistency across multiple test intervals, the motors and magnetometers were rigidly mounted to a

115   nonmagnetic plate, which was in turn mounted inside the Merritt coil. Special 3D-printed mounts were designed for both the simulated reaction wheels and magnetometers to enable proper alignment with the coil system and each other. Figure 4 provides a photograph of the integrated setup (left) and a technical drawing of the total apparatus (right). Figure 4a shows the four Twinleaf VMR magnetometers used, mounted in a practical configuration similar to a typical gradiometer scheme. This configuration also enables users to test interference mitigation algorithms with various magnetometer suite topologies, which

120   can be useful for application to missions that do not utilize a traditional co-linear gradiometer configuration (e.g., the upcoming HERMES NEMISIS magnetometers). Figure 4b shows the two simulated reaction wheels, seen in greater detail in Fig. 3. The Merritt coil used to generate large magnetic trends is partially shown in Fig. 4c. The large rectangular object between the Twinleaf VMRs and simulated reaction wheels is a reference magnetometer used during initial testing and setup of the coil system and is not relevant to the output dataset. The technical drawing provides measurements, in meters, referenced against

125   the coil system. The sensors are located near the center of the coil system and should therefore be within the region of assumed homogeneity. Note that the labels M_1 – M_4 on the technical drawing correspond to the labels associated with each magnetometer in the output dataset.
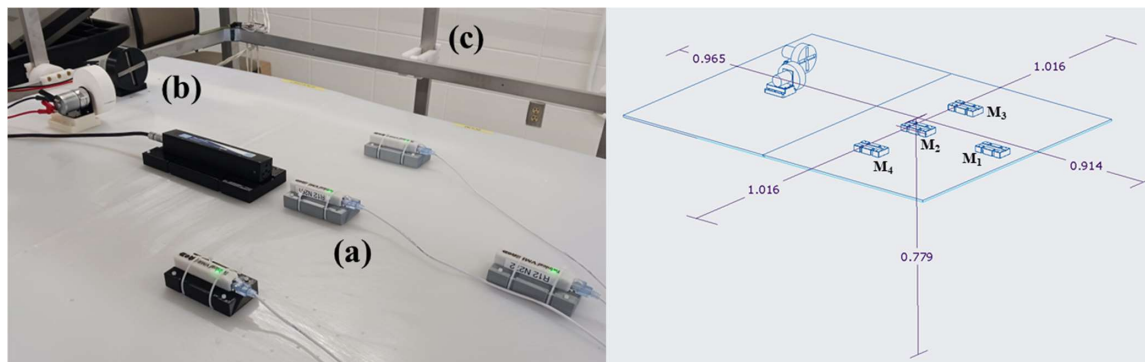
Figure 4: Experimental setup used for data collection. (Left) Photograph of experimental setup. (a) Four Twinleaf VMR magnetometers used to capture magnetic field data; (b) DC motors with attached ferromagnetic plates, used to simulate spacecraft reaction wheels; (c) Merritt coil system used to simulate geophysical fields. (Right) Schematic of experimental setup with measurements, in meters, referenced to the Merritt coil system.

3 Captured Data

This section provides details of the data collection and processing steps taken in the generation of this dataset. Note that all applied voltages discussed in this section are in units of V_{RMS}.

3.1 Data Acquisition

Following the deployment of the experimental setup in the coil system, various stimuli were applied to serve as proxies for the Earth's magnetic field, magnetic interference, and geophysical signals as seen by an orbiting spacecraft. Table 1 describes the different stimuli applied to the Merritt coil system (discussed in Sec. 2.2) used to generate the large, near-DC field serving as a proxy for Earth's magnetic field. Table 2 describes the stimuli applied to the motors (discussed in Sec. 2.3) used to generate physically-synthesized reaction wheel interference. Table 3 describes the stimuli, applied to the coil formers and within the coil system, used to create pseudo-geophysical wave packets and signals.

Table 1: Description of the stimulus applied to generate near-DC trends as a proxy for Earth's magnetic field.

Near-DC Trend	
Label	**Stimulus Description**
Trend1	0.001 Hz sine wave with 20 V amplitude applied to coil system X-axis.
Trend2	0.003 Hz sine wave with 10 V amplitude applied to coil system Y-axis.
Trend3	0.002 Hz sine wave with 25 V amplitude applied to coil system Z-axis.
Trend4	0.001 Hz sine waves with 15 V amplitude applied to X-, Y-, Z- axes; Phase offset $\varphi = 0º, 30º, 90º$, respectively.

Trend5	0.001 Hz sine waves with 20 V amplitude applied to X-, Y-, Z- axes with no phase offsets.

145 **Table 2: Description of the stimulus applied to generate magnetic interference as a proxy for spacecraft reaction wheels. Variable voltages induce variable speeds, simulating spacecraft maneuvers.**

Interference	
Label	**Stimulus Description**
Inter1	Motor 1 & 2 driven at 2.5 V for duration.
Inter2	Motor 1 & 2 driven at 5 V for duration.
Inter3	Motor 1 driven at 3 V for duration.
	Motor 2 driven at 2.5 V for duration.
Inter4	Motor 1 driven at 5 V for start. After ~15-min, adjust down to 4 V.
	Motor 2 driven at 4 V for duration.
Inter5	Motor 1 driven at 5 V for duration.
	Motor 1 driven at 5 V for start. After ~15-min, adjust up to 7.5 V, then down to 2.5 V, then back to 5 V.
Inter6	Motor 1 & 2 start at 7.5 V. After ~10-min, adjust down to 2.5 V. After ~20-min, adjust up to 6 V.
Inter7	Motor 1 driven at 7 V for duration.
	Motor 2 driven at 6 V for duration.
Inter8	Motor 1 driven at 3 V for start. After ~10-min, adjust up to 8 V.
	Motor 2 driven at 8 V for duration.

Table 3: Description of the stimulus applied to generate interesting magnetic phenomena as a proxy for geophysical signals.

Geophysical Signals	
Label	**Stimulus Description**
GeoSignal1	0.75 Hz sinusoid applied to X-axis coil former with amplitude swept from 0 V to 0.6 V_{rms} to 0 V.
	Stimulus applied at ~10-min and ~20-min.
GeoSignal2	0.2 V_{rms} sinusoid applied to X-axis coil former with frequency swept from 0.75 Hz to 20 Hz.
	Stimulus applied at ~10-min and ~20-min.
GeoSignal3	5.0 Hz sinusoid applied to X-axis coil former with amplitude swept from 0 V to 0.6 V_{rms} to 0 V.
	Stimulus applied at ~10-min and ~20-min.
GeoSignal4	10.0 Hz sinusoid applied to X-axis coil former with amplitude swept from 0 V to 0.6 V_{rms} to 0 V.
	Stimulus applied at ~10-min and ~20-min.
GeoSignal5	Vigorous ferromagnetic wrench-waving inside coil system performed by exemplary postdoc.
	Stimulus applied at ~5, 10, 15, 20, and 25-min.

GeoSignal6	0.1 V_{rms} sinusoid applied to X-axis coil former with frequency swept from 0.75 Hz to 20 Hz. Stimulus applied at ~8, 16, and 24-min.

150 **3.2 Data Processing**

The data exported by the Twinleaf I/O software is considered the Level 0 data product. This consists of a tab separated value (i.e., *.tsv*) file, containing vector data from each of the four magnetometers, for each capture interval. The remainder of this section will discuss the data product processing pipeline necessary to convert this into a maximally useful dataset for the validation of magnetic field interference mitigation algorithms. Note that intermediary processing steps (i.e., Level 1 and 2a)

155 output data in a standard MATLAB v7 data format (*.mat*) for ease of readability by a variety of programs, but the final output (i.e., Level 2b) is stored in an ISTP-compliant Common Data Format file (*.cdf*).

3.2.1 Level 1 – Filtering and Truncation

Level 1 data processing considers the measurements associated with each data category (i.e., near-DC trend, simulated interference, and pseudo-geomagnetic phenomena) independently. The Level 0 data files are first read in, parsed, and filtering

160 steps appropriate for each type of data are applied.

As discussed in Sec. 2.2, the Merritt coil system produces fairly egregious amplitude steps when driven at frequencies less than ~1 Hz. Therefore, a 0.1 Hz low-pass filter is applied to each instance of the near-DC data described in Table 1. This filtering reduces the impact of the amplitude steps, although some ringing is still apparent in the output. The simulated reaction wheel interference captured as described in Table 2 contains near-DC offsets from various static and time-varying local sources

165 (including the building's elevators, nearby cars, and hard-working postdocs carrying ferromagnetic objects). The sinusoidal simulated interference data was brought down to a near-zero mean by subtracting a 20-second sliding average from the original data. The simulated small-scale geophysical signals described in Table 3 have no filtering applied during this stage, as spontaneous magnetic perturbation from uncontrolled sources enhance the purpose of this data product. Finally, each interval captured is truncated to a length of 30-min, starting after 30 seconds, to avoid edge artifacts caused by the filtering process.

170 **3.2.2 Level 2a – Data Combination**

Level 2a data processing considers the possible combinations of Level 1 data that result in useful representations of in-situ spacecraft magnetometer measurements, enabling validation of practical interference mitigation techniques. The Level 2a data processing step results in several distinct 30-min intervals of magnetometer measurements for each broad category of data collected. Specifically, five intervals of near-DC trend, eight intervals of synthetic reaction wheel interference, and six

175 intervals of pseudo-geomagnetic phenomena. This results in 120 hours of possible combinations when combining a single interval from each category. Additional intervals of Level 2a data can be generated by utilizing multiple intervals from each category, which also serves to increase the potential data complexity.

It should be noted that a common assumption for in-situ measurements is that geophysical magnetic fields will be identical at all scientific magnetometers onboard the spacecraft, whereas the interference measured by the sensors will fall off

180   distance from the body of the spacecraft. As such, when combining the data only measurements from one of four magnetometers is used for the near-DC trend and geomagnetic phenomena. However, for the synthetic reaction wheel interference all four magnetometer measurements are utilized.
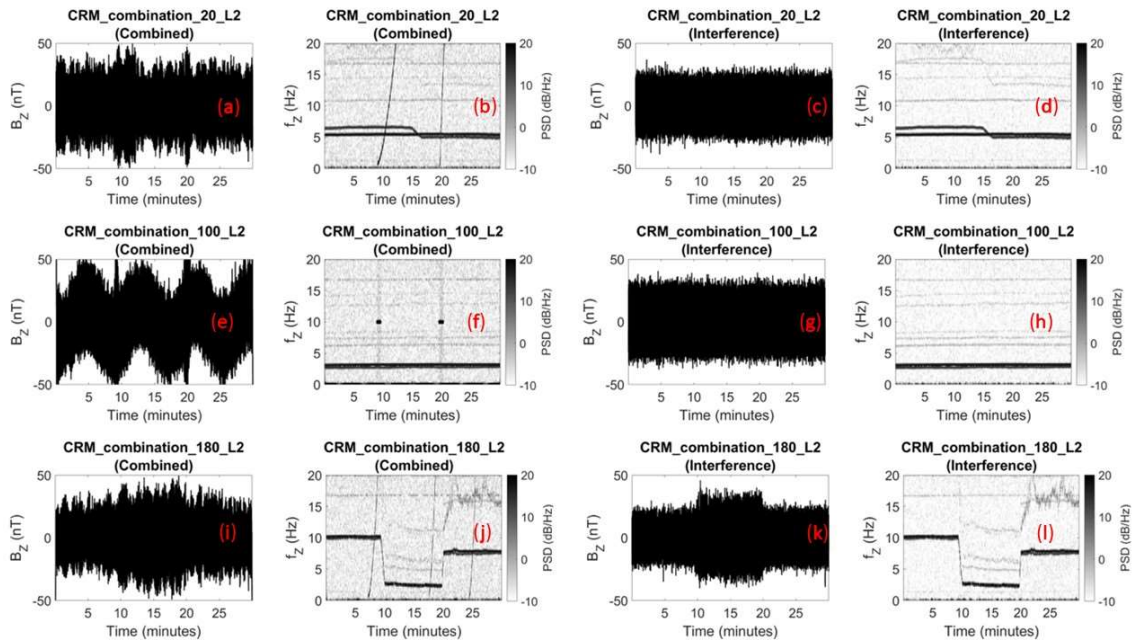
Figure 5: Sample intervals captured by M₂ in laboratory-generated dataset. (Column 1-2) Detrended time series and spectra

185   **associated with the combined data product; (Columns 3-4) Time series and spectra corresponding to the ground truth interference; (Rows) Individual sample intervals.**

3.2.3 Level 2b – CDF Conversion

Level 2b data processing involves the transformation of the combined data generated in Level 2a into Common Data Format (*.cdf*) for enhanced accessibility and usability within the space research community. The use of .cdf files is a common

190   practice in space research, with NASA's support ensuring widespread compatibility and longevity.

Each converted *.cdf* file contains all the essential variable information and metadata required to understand and use the data. Each file contains 16 variables corresponding to the measurements of the combined signal, interference signal, near DC-trend signal, and pseudo-geomagnetic signal for each magnetometer, separated into the sensors' x, y, and z magnetic components. Figure 5 illustrates several example data contained in the dataset. Each row in Fig. 5 corresponds to a different

195   combination of trend, pseudo-geomagnetic signal, and interference. The time series for these combinations are shown in the first column of Fig. 5, with the associated spectra shown in column two. Note that the combined data has been detrended with a twenty-second moving average for ease of visualization. The interference to be identified and removed, along with its associated spectra, is shown in the third and fourth columns of Fig. 5, respectively. Rows one and three illustrate combinations that have variable motor rates, which is a simulation of conditions seen during spacecraft maneuvers. Their associated

200   interference is a frequency-swept wave packet simulating geophysical phenomena such as whistler-mode waves. The second row of Fig. 5 provides a similar example, but with fixed motor rates and an amplitude-modulated wave packet applied at a fixed frequency.

          Figure 6 provides an illustration of the variables contained in a single *.cdf* file, along with some of the informative metadata describing the variable. In this case, the highlighted variable is *InterMag1*, the interference signal, measured by **M1**

205   in *CRM_combination_20_L2*. It can be seen from the descriptor text near the bottom of Fig. 6 that the interference for this piece of data was generated from two motors. First, motor 1 is driven at 5V. After ~15 minutes, it was adjusted down to 4 V. Motor 2 was driven at 4 V for the total duration. The graphical output shown in Fig. 6 is from the Autoplot software, a useful tool for rapidly parsing, visualizing, and analyzing *.cdf* files. Autoplot is fully compatible with the dataset presented in this manuscript, and more information about the software is available at http://www.autoplot.org.
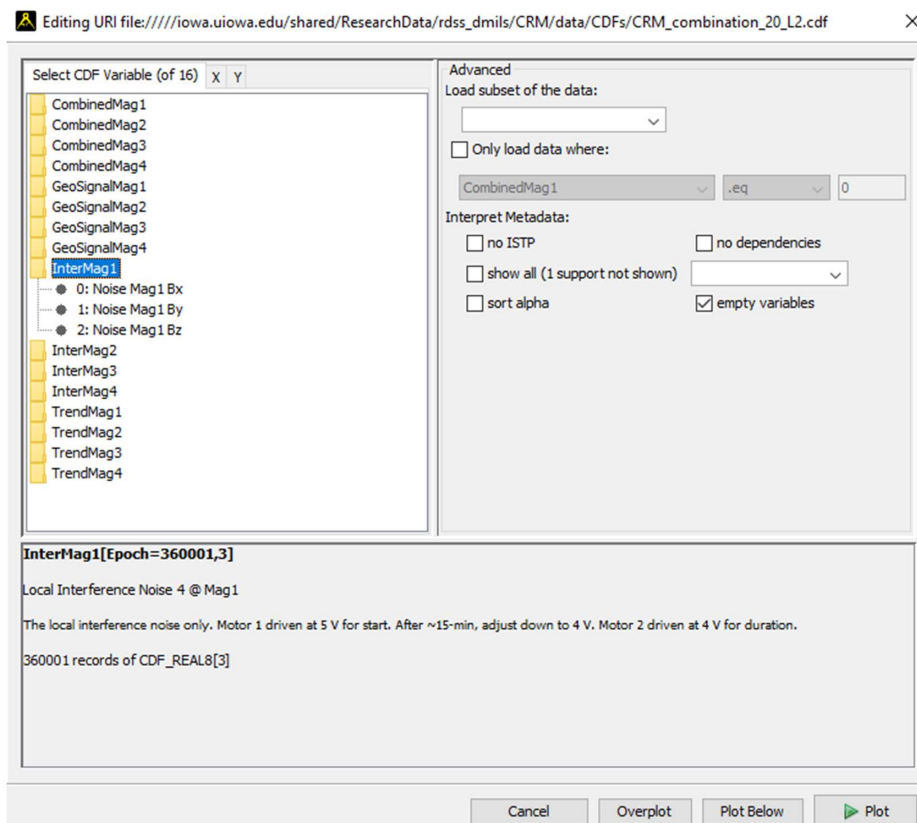
210

Figure 6: CDF variable information associated with a single data combination. In total, each CDF contains 16 variables, four for each magnetometer. Each magnetometer has measurements associated with near-DC trend, physically-synthesized interference signal, a pseudo-geophysical signal, and the combination of these constituent components. Each magnetometer measurement contains an x, y, and z component.

215 **4 Discussion and Future Work**

The primary objective of this dataset is to function as a validation tool for existing and future interference mitigation algorithms. It provides a clear distinction between interference and pseudo-geophysical signals, establishing a reliable ground truth for the validation of these algorithms. However, this section outlines several potential avenues for future work in the further development of this dataset.

220 Firstly, the dataset can be extended into more complex and challenging scenarios. Although the data presented in this manuscript has only combined a single interference signal with a single pseudo-geophysical signal and near-DC trend, combinations of multiple interference signals or multiple pseudo-geophysical signals can be generated that may be more

difficult for some interference mitigation schemes. Additionally, the data can be time-shifted to provide more substantial spectral overlap between the pseudo-geophysical signal and interference, which is a common and challenging problem when

225   attempting to mitigate local magnetic interference. Finally, this dataset has only provided physically synthesized proxies for a single type of local magnetic interference (i.e., reaction wheels). Although this is often a dominant source of interference on many spaceflight missions, it is not the only source of interference seen in in-situ magnetic field measurements. Spacecraft heaters, magnetic torque rods, and electrical currents from subsystems such as solar panels are commonly present in magnetometer data (Angelini et al., 2022; Stolle et al., 2021). Physical proxies for these interference sources can also be

230   generated and added to the dataset, providing a more thorough set of example data for use in the validation of interference mitigation techniques.

It should also be noted that, although this work is intended to support interference mitigation efforts for spaceflight missions, many other fields that utilize magnetometry suffer from local magnetic interference when taking measurements. For example, many geological and archaeological surveys have begun to deploy unmanned aerial vehicles (UAVs) equipped with

235   gradiometric magnetometer arrays to perform subsurface mapping (Zheng et al., 2021). These UAVs generate substantial local magnetic field (e.g., from their rotors, motors, and other subsystems), contaminating the measurements being taken. One common approach to mitigating these interfering local fields is to deploy the magnetometer arrays far from the UAV via a system of tethers. However, these tethers can cause additional complications when the UAV must traverse complex terrain or fly at low altitudes, and as a result more complex interference mitigation techniques must be utilized (Kaub et al., 2021). These

240   complications are not limited to low-altitude unmanned aerial surveys, but also apply to higher-altitude manned aeromagnetic surveying (Tuck et al., 2021). One dominant source of interference seen in these various aerial magnetic surveys are the time-varying fields generated by the spinning motors onboard the aircraft (Lee et al., 2020), similar to the spinning reaction wheels used to control a spacecraft's attitude that are physically synthesized in the dataset presented in this manuscript. It can be seen that, due to the similarities between the magnetic signatures of dominant interference sources, this work can easily serve to

245   validate interference mitigation efforts across a wide range of fields.

5 Conclusion

In our pursuit of comprehending physical processes throughout near-Earth space and our solar system, in-situ magnetometer measurements stand as indispensable tools. Despite recent advancements in magnetometer technology, interference from spacecraft-generated magnetic fields often contaminate our scientific measurements. Historically, this

250   interference was mitigated using a traditional gradiometric applied to two or more sensors deployed along a long boom. Many recent missions have opted for shorter booms to reduce cost and technical complexity, which also reduces the effectiveness of classical gradiometry. As a result, novel approaches for the mitigation of local magnetic interference from the spacecraft have emerged, but the quantification of their performance remains challenging due to the lack of available ground-truth data. This manuscript has presented a dataset to enable the rigorous analysis of these techniques by generating and measuring various

255 magnetic phenomena representative of those seen by in-situ spacecraft. Specifically, ten hours of data containing near-DC trends, physically-synthesized interference, and pseudo-geophysical signals have been simultaneously captured by four magnetometers and combined to provide over 100 hours of measurements that can be used as a testbed for interference mitigation schemes. This dataset also provides a ground truth for the magnetic interference, enabling rigorous quantification of an algorithm's performance.

260 **Code & Data Availability**

The dataset presented in this manuscript is currently available at https://iowa-my.sharepoint.com/:f:/g/personal/amflores_uiowa_edu/ElhGXdssbtJFtaROKpndzuQBaX9-1nckRsluCtD0DD37aQ?e=CvjQ4H. Upon acceptance of this manuscript, the dataset, and code used to generate it, will be moved to a University of Iowa Institutional Repository for long-term storage and reuse.

265 **Author Contribution**

Finley and Miles conceptualized the project. Morris, Broadfoot, and Hisel developed the test setup. Finley, Flores, Homann, and Piker captured the data. Finley and Piker wrote the software to produce the output data product and associated metadata. Finley, Flores, and Broadfoot wrote the manuscript. All authors contributed to the proofreading of the manuscript. Miles and Sen Gupta were responsible for funding acquisition and project management.

270 **Competing Interests**

The authors declare that they have no conflict of interest.

Acknowledgements

This work was supported in part by the US Air Force Office of Scientific Research under grant FA9550-21-1-0206. M.G. Finley was additionally supported for this work in part by the National Aeronautics and Space Administration HERMES
275 mission and grants 80NSSC21M0180, 80NSSC23K1295.

References

280 Angelini, V., O'Brien, H., Horbury, T., & Fauchon-Jones, E. (2022). Novel magnetic cleaning techniques for Solar Orbiter magnetometer. *2022 ESA Workshop on Aerospace EMC (Aerospace EMC)*, 1–6. https://doi.org/10.23919/AerospaceEMC54301.2022.9828828

Bale, S. D., Goetz, K., Harvey, P. R., Turin, P., Bonnell, J. W., Dudok de Wit, T., Ergun, R. E., MacDowall, R. J., Pulupa, M., Andre, M., Bolton, M., Bougeret, J.-L., Bowen, T. A., Burgess, D., Cattell, C. A., Chandran, B. D. G., Chaston, C.

285 C., Chen, C. H. K., Choi, M. K., … Wygant, J. R. (2016). The FIELDS Instrument Suite for Solar Probe Plus. *Space Science Reviews*, *204*(1), 49–82. https://doi.org/10.1007/s11214-016-0244-5

Bowen, T. A., Mallet, A., Huang, J., Klein, K. G., Malaspina, D. M., Stevens, M., Bale, S. D., Bonnell, J. W., Case, A. W., Chandran, B. D. G., Chaston, C. C., Chen, C. H. K., Dudok de Wit, T., Goetz, K., Harvey, P. R., Howes, G. G., Kasper, J. C., Korreck, K. E., Larson, D., … The PSP/FIELDS and PSP/SWEAP Teams. (2020). Ion-scale

290 Electromagnetic Waves in the Inner Heliosphere. *The Astrophysical Journal Supplement Series*, *246*(2), 66. https://doi.org/10.3847/1538-4365/ab6c65

Broadfoot, R. M., Miles, D. M., Holley, W., & Howarth, A. D. (2022). In situ calibration of the Swarm-Echo magnetometers. *Geoscientific Instrumentation, Methods and Data Systems*, *11*(2), 323–333. https://doi.org/10.5194/gi-11-323-2022

Burt, J., Goans, M., Blackwood, J., & Brown, K. (2022). Heliophysics Environmental & Radiation Measurement Experiment

295 Suite (HERMES): A Small External Payload for Gateway with Big Challenges. *2022 IEEE Aerospace Conference (AERO)*, 1–11. https://doi.org/10.1109/AERO53065.2022.9843491

Clagett, C., Santos, L., Azimi, B., Cudmore, A., Marshall, J., Starin, S., Sheikh, S., Zesta, E., Paschalidis, N., Johnson, M., Kepko, L., Berry, D., Bonalsky, T., Chai, D., Colvin, M., Evans, A., Hesh, S., Jones, S., Peterson, Z., … Rodriquez, M. (2017). Dellingr: NASA Goddard Space Flight Center's First 6U Spacecraft. *Small Satellite Conference*.

300 https://digitalcommons.usu.edu/smallsat/2017/all2017/83

Connerney, J. E. P., Benn, M., Bjarno, J. B., Denver, T., Espley, J., Jorgensen, J. L., Jorgensen, P. S., Lawton, P., Malinnikova, A., Merayo, J. M., Murphy, S., Odom, J., Oliversen, R., Schnurr, R., Sheppard, D., & Smith, E. J. (2017). The Juno Magnetic Field Investigation. *Space Science Reviews*, *213*(1), 39–138. https://doi.org/10.1007/s11214-017-0334-z

Connerney, J. E. P., Espley, J., Lawton, P., Murphy, S., Odom, J., Oliversen, R., & Sheppard, D. (2015). The MAVEN
305   Magnetic Field Investigation. *Space Science Reviews*, *195*(1), 257–291. https://doi.org/10.1007/s11214-015-0169-4

Constantinescu, O. D., Auster, H.-U., Delva, M., Hillenmaier, O., Magnes, W., & Plaschke, F. (2020). Maximum-variance
gradiometer technique for removal of spacecraft-generated disturbances from magnetic field data. *Geoscientific
Instrumentation, Methods and Data Systems*, *9*(2), 451–469. https://doi.org/10.5194/gi-9-451-2020

Finley, M. G., Bowen, T. A., Pulupa, M., Koval, A., & Miles, D. M. (2023). Statistical Decomposition and Machine Learning
310   to Clean In Situ Spaceflight Magnetic Field Measurements. *Geophysical Research Letters*, *50*(13), e2023GL103626.
https://doi.org/10.1029/2023GL103626

Finley, M. G., Broadfoot, R. M., Shekhar, S., & Miles, D. M. (2023). Identification and Removal of Reaction Wheel
Interference From In-Situ Magnetic Field Data Using Multichannel Singular Spectrum Analysis. *Journal of
Geophysical Research: Space Physics*, *128*(2), e2022JA031020. https://doi.org/10.1029/2022JA031020

315   Gordon, D., & Brown, R. (1972). Recent advances in fluxgate magnetometry. *IEEE Transactions on Magnetics*, *8*(1), 76–82.
https://doi.org/10.1109/TMAG.1972.1067268

Greene, K., Hansen, C., Narod, B. B., Dvorsky, R., & Miles, D. M. (2022). Tesseract – a high-stability, low-noise fluxgate
sensor designed for constellation applications. *Geoscientific Instrumentation, Methods and Data Systems*, *11*(2), 307–
321. https://doi.org/10.5194/gi-11-307-2022

320   Hoffmann, A. P., & Moldwin, M. B. (2022). Separation of Spacecraft Noise From Geomagnetic Field Observations Through
Density-Based Cluster Analysis and Compressive Sensing. *Journal of Geophysical Research: Space Physics*, *127*(9),
e2022JA030757. https://doi.org/10.1029/2022JA030757

Imajo, S., Nosé, M., Aida, M., Matsumoto, H., Higashio, N., Tokunaga, T., & Matsuoka, A. (2021). Signal and Noise
Separation From Satellite Magnetic Field Data Through Independent Component Analysis: Prospect of Magnetic
325   Measurements Without Boom and Noise Source Information. *Journal of Geophysical Research: Space Physics*,
126(5), e2020JA028790. https://doi.org/10.1029/2020JA028790

Kaub, L., Keller, G., Bouligand, C., & Glen, J. M. G. (2021). Magnetic Surveys With Unmanned Aerial Systems: Software for Assessing and Comparing the Accuracy of Different Sensor Systems, Suspension Designs and Compensation Methods. *Geochemistry, Geophysics, Geosystems*, *22*(7), e2021GC009745. https://doi.org/10.1029/2021GC009745

330 Langel, R., Ousley, G., Berbert, J., Murphy, J., & Settle, M. (1982). The MAGSAT mission. *Geophysical Research Letters*, *9*(4), 243–245. https://doi.org/10.1029/GL009i004p00243

Lee, H., Lee, C., Jeon, H., Son, J. J., Son, Y., & Han, S. (2020). Interference-Compensating Magnetometer Calibration With Estimated Measurement Noise Covariance for Application to Small-Sized UAVs. *IEEE Transactions on Industrial Electronics*, *67*(10), 8829–8840. https://doi.org/10.1109/TIE.2019.2950841

335 Merritt, R., Purcell, C., & Stroink, G. (1983). Uniform magnetic field produced by three, four, and five square coils. *Review of Scientific Instruments*, *54*(7), 879–882. https://doi.org/10.1063/1.1137480

Miles, D. M., Ciurzynski, M., Barona, D., Narod, B. B., Bennest, J. R., Kale, A., Lessard, M., Milling, D. K., Larson, J., & Mann, I. R. (2019). Low-noise permalloy ring cores for fluxgate magnetometers. *Geoscientific Instrumentation, Methods and Data Systems*, *8*(2), 227–240. https://doi.org/10.5194/gi-8-227-2019

340 Miller, D. C. (1979, April 1). *The Voyager magnetometer boom*. https://ntrs.nasa.gov/citations/19790013187

Ness, N. F., Behannon, K. W., Lepping, R. P., & Schatten, K. H. (1971). Use of two magnetometers for magnetic field measurements on a spacecraft. *Journal of Geophysical Research (1896-1977)*, *76*(16), 3564–3573. https://doi.org/10.1029/JA076i016p03564

Paterson, W. R., Gershman, D. J., Kanekal, S. G., Livi, R., Moldwin, M. B., Zesta, E., Randol, B., & Samara, M. (2023).

345 *Heliospheric Science From Gateway With HERMES * (EGU23-8425). EGU23. Copernicus Meetings. https://doi.org/10.5194/egusphere-egu23-8425

Sen Gupta, A., & Miles, D. (2023). Autonomous Reaction Wheel Magnetic Signature Detection Against Background Noise in Spacecraft. *IEEE Sensors Letters*, *7*(11), 1–4. https://doi.org/10.1109/LSENS.2023.3308124

Stolle, C., Michaelis, I., Xiong, C., Rother, M., Usbeck, Th., Yamazaki, Y., Rauberg, J., & Styp-Rekowski, K. (2021).

350 Observing Earth's magnetic environment with the GRACE-FO mission. *Earth, Planets and Space*, *73*(1), 51. https://doi.org/10.1186/s40623-021-01364-w

Styp-Rekowski, K., Michaelis, I., Stolle, C., Baerenzung, J., Korte, M., & Kao, O. (2022). Machine learning-based calibration of the GOCE satellite platform magnetometers. *Earth, Planets and Space*, *74*(1), 138. https://doi.org/10.1186/s40623-022-01695-2

355 Tuck, L. E., Samson, C., Laliberté, J., & Cunningham, M. (2021). Magnetic interference mapping of four types of unmanned aircraft systems intended for aeromagnetic surveying. *Geoscientific Instrumentation, Methods and Data Systems*, *10*(1), 101–112. https://doi.org/10.5194/gi-10-101-2021

Wallis, D. D., Miles, D. M., Narod, B. B., Bennest, J. R., Murphy, K. R., Mann, I. R., & Yau, A. W. (2015). The CASSIOPE/e-POP Magnetic Field Instrument (MGF). *Space Science Reviews*, *189*(1), 27–39. https://doi.org/10.1007/s11214-014-
360 0105-z

Zheng, Y., Li, S., Xing, K., & Zhang, X. (2021). Unmanned Aerial Vehicles for Magnetic Surveys: A Review on Platform Selection and Interference Suppression. *Drones*, *5*(3), Article 3. https://doi.org/10.3390/drones5030093